CrossMark

Spatial characteristics of ocean surface waves

**Johannes Gemmrich[1] · Jim Thomson[2] · W. Erick Rogers[3] · Andrey Pleskachevsky[4] ·
Susanne Lehner[4]**

Abstract The spatial variability of open ocean wave fields
on scales of O (10km) is assessed from four different data
sources: TerraSAR-X SAR imagery, four drifting SWIFT
buoys, a moored waverider buoy, and WAVEWATCH III
® model runs. Two examples from the open north-east
Pacific, comprising of a pure wind sea and a mixed sea
with swell, are given. Wave parameters attained from obser-
vations have a natural variability, which decreases with
increasing record length or acquisition area. The retrieval of
dominant wave scales from point observations and model
output are inherently different to dominant scales retrieved
from spatial observations. This can lead to significant dif-
ferences in the dominant steepness associated with a given
wave field. These uncertainties have to be taken into account
when models are assessed against observations or when
new wave retrieval algorithms from spatial or temporal data
are tested. However, there is evidence of abrupt changes in
wave field characteristics that are larger than the expected
methodological uncertainties.

1 Introduction

The random, multi-scale characteristics of wave fields at
the surface of oceans and lakes are commonly described
by a small set of wave parameters. These parameters are
based on statistical properties of the wave field, like signif-
icant wave height H_s, which is defined as the mean of the
one third highest waves or spectral properties of the most
energetic wave scales, like dominant wave length λ_p, speed
c_{pk} or period T_p, and dominant direction θ_p. These scales
are the scale of the maximum of the energy spectrum and,
therefore, are also termed the 'peak' wave scales. The vast
majority of wave observations are obtained as time series of
surface elevation, pressure, or orbital velocities at a single
location. Most commonly, wave observations are obtained
from surface following floats equipped with accelerometers
or global positioning devices (GPS). However, a variety of
measuring devices has been developed over the last 60
years, or so, ranging from bottom-mounted and sub-surface
moorings, like pressure sensors and acoustic Doppler cur-
rent profilers (ADCPs), to acoustic or optical range-gauging
sensors mounted on platforms or ships tens of metres above
the surface. The underlying basic principle to all these
devices is that the wave field parameters are defined as
quantities obtained during a finite measuring period, and the
wave field is assumed to be stationary over this period. This
acquisition period is not universally agreed on, but usually
lies in the range of 20 to 40 min. Operational networks of

✉ Johannes Gemmrich
gemmrich@uvic.ca

[1]   University of Victoria, Physics and Astronomy, PO Box 1700,
Victoria, BC, V8W 2Y2, Canada

[2]   Applied Physics Laboratory, Seattle, WA, USA

[3]   Naval Research Laboratory, Stennis Space Center,
MS, USA

[4]   German Aerospace Centre - DLR, Bremen, Germany

wave buoy observations are concentrated in a band of about 500 km width along the coast with typical spacing of O (100km), (see e.g., National Data Buoy Center, www.ndbc.noaa.gov).

Alternatively, wave field characteristics may also be derived from a snapshot of the surface elevation over a large enough spatial extent that allows reliable statistics of all relevant wave scales. Scanning the water surface with the required spatial coverage and resolution can be achieved with marine X-band radars, coastal HF radars, and airborne or space-borne synthetic aperture radar (SAR). As data from this type of observations become more prevalent, new insight on the variability of wave fields over spatial scales of a few tens of kilometers will be gained. This will have implications ranging from the comparison of sea state parameters derived in frequency or wavenumber space to the apparent occurrence rate of extreme waves (Heller 2006; Gemmrich and Garrett 2011).

Here, we compare the spatial variability of sea state parameters in the open ocean obtained from three different sources: space-borne SAR images, a set of closely spaced buoys, and a widely used wave model, WAVEWATCH III ® (Tolman and the WAVEWATCH III Development Group 2014) (in the following: TWDG2014).

2 Methods

We are interested in the spatial stationarity of wave fields away from coastal or heterogeneous, strong atmospheric influences. Wave, wind, and surface layer turbulence data were collected in the vicinity of OceanWeather Station P at 50 N, 145 W during a mooring turnaround cruise in January 2015 aboard the R/V T. G. Thompson. There were two TerraSAR-X overpasses coinciding with the in situ observations at Station P. Wind observations were made with a 3-axis sonic anemometer mounted to the jackstaff at the bow of the ship at 16 m height above the surface. More information about additional measurements, and in particular the energy input into and dissipation of the wave field can be found in Thomson et al. (2016).

2.1 Wave retrieval from synthetic aperture radar SAR

Over the ocean, synthetic aperture radar is capable of providing wind and wave information by measuring the roughness of the sea surface. In particular, TerraSAR-X data have been used to investigate the highly variable wave climate in coastal areas (Bruck and Lehner 2013; Lehner et al. 2014). In addition, TerraSAR-X data provide accurate estimates of the wind field over the ocean.

TerraSAR-X operates in the X-band with 31-mm wavelength from 15 sun-synchronous orbits per day at 514

km, yielding a repeat-cycle of 11 days. However, by varying the incidence angle repeat coverage at mid-latitude locations can be achieved approximately every 3 days, and more frequently in polar regions. The low altitude, short wave length, and high resolution of TerraSAR-X are advantageous for the retrieval of meteo-marine parameters, compared to previous satellite-based SAR systems.

The TerraSAR-X data used for this study are Multi-Look Ground Range Detected (MGD) standard products. We use VV-polarization in the so-called StripMap mode, which covers a 30-km wide swath at a pixel spacing of 1.25 m. Details on the conversion of image intensity to normalized radar cross section σ_0 can be found in Pleskachevsky et al. (2016).

The retrieval of wind speeds from TerraSAR-X data is based on the XMOD algorithm (Ren et al. 2012). The normalized radar cross section σ_0 is a function of the incidence angle α, the wind direction ϕ relative to the SAR flight direction, and the wind speed U.

$$\sigma_o = a_o + a_1 U + a_2 \sin(\alpha) + (a_3 + a_4 U)\cos(2\phi), \qquad (1)$$

where $a_0 ... a_4$ are empirical constants. Calibration of the observed radar backscatter, i.e., the image brightness, yields σ_0 (in decibel), and the wind speed U is calculated solving (1) iteratively. The wind direction can be retrieved directly from the SAR image (e.g, Koch (2004)) or taken from nearby in situ observations or other independent sources. Here, we take the results from the atmospheric model providing the wind input for the wave model.

At the same time, the corresponding sea state can be estimated from the same image. The empirical X-WAVE model function for obtaining integrated wave parameters from X-band data has been developed for deep water (Bruck and Lehner 2013; Bruck 2015). Here, we use a reduced version of the original model function X-WAVE to estimate the significant wave height

$$H_s = A_0(\beta) + A_1\sqrt{E \tan(\alpha)}, \qquad (2)$$

where A_0, A_1 are empirical coefficients. The varying degrees of non-linear imaging distortion inherent in SAR-observations are accounted for by the dependence on β, the angle between the dominant wave direction, and the satellite azimuth, i.e. flight direction ($0^o \leq \beta \leq 90^o$). For a detailed discussion of TerraSAR-X imaging artifacts, see Pleskachevsky et al. (2016).

The parameter E is an integral measure of the scaled radar backscatter

$$\tilde{\sigma} = \frac{\sigma_o}{\bar{\sigma}_o} - 1 : \qquad (3)$$

$$E = \int_{k_1}^{k_2} \int_0^{2\pi} P(k, \theta)dkd\theta, \qquad (4)$$

where P is the 2-d power spectrum of $\tilde{\sigma}$. The wave number integration limits k_1, k_2 correspond to wave lengths between 500 m and 30 m. TerraSAR-X flies at an orbit of 514 km, which is lower than most space-borne SAR sensors, resulting in relatively weak SAR-specific imaging artefacts. Nevertheless, to remove the energy associated with potential image distortions, the 2-D power spectrum is scaled in a way that the 1-d wave number spectrum

$$S(k) = \int_0^{2\pi} P(k,\theta)d\theta \;\; \propto \; k^{-3}, \tag{5}$$

for $1.5k_p < k < k_2$, where k_p is the wave number associated with the dominant wave scale, in case of a single-peaked wave spectrum. For double-peaked spectra k_p is associated with the dominant wind sea (Fig. 1), defined as the spectral peak in the actively forced spectral range $k < g/U^2$, corresponding to spectral wave ages $c_p/U < 1$, with phase speed c_p.

The constants A_0, A_1 have been tuned to match H_s observations over NDBC wave buoys. The dominant wave lengths and wave direction are given by the maximum

Fig. 1 Spectra of TerraSAR-X sub-scene centred at 50.03^oN, 145.12^oW on 5 January 2015. **a** 2-D wavenumber spectrum. *Circles* correspond to wave lengths of 30, 50, 100, 200m (*decreasing radius*). **b** 1-D wavenumber spectrum (*line*) and dominant wave scale (*circle*). High wavenumbers are scaled to obey theoretical dependence (*black*). Raw spectrum is shown in gray. **c** 1-D frequency spectrum. The *dashed line* indicates a ω^{-4} dependence, the *circle* the dominant frequency of the wind-sea

value of the 2-D image wavenumber spectrum. Utilizing the deep-water wave dispersion relation without currents

$$\omega^2 = gk \tag{6}$$

with wave frequency $\omega = 2\pi f$ and gravitational acceleration g, the spectrum can be converted into frequency space.

Wave parameters are obtained from sub-scenes of the SAR image. Typically, we downsample the TerraSAR-X stripmap image to a 2.5 m pixel resolution, and base the wave and wind retrieval on consecutive 1024×1024 pixel scenes. To increase spectral resolution, and to reduce aliasing effects, the sub-scenes are centered within a zero-padded 2048×2048 array. Thus, wave parameters are derived at a spatial resolution of approximately 2.5 km. The sensitivity of the results on the choice of the sub-scene size is discussed in Section 4. The 180° ambiguity of the SAR spectra (Fig. 1a) can be resolved with complex data or estimated from the image directly (Koch 2004). Here, we simply chose the peak closest to the wind direction.

2.2 In situ wave buoy observations

A suite of instruments called SWIFT (Surface Wave Instrument Floats with Tracking) has been developed to observe wave breaking and turbulence close to the surface in a wave-following frame of reference (Thomson 2012). SWIFT's are freely floating and are designed to follow the free surface. GPS sensors in the hull collect velocities and heave accelerations at 4 Hz, from which surface elevation time series and directional information are obtained (Herbers et al. 2012). Data segments of 30 min are used to estimate significant wave heights and 1-d frequency spectra. Here, up to 4 SWIFTs have been deployed within the TerraSAR-X image coverage, or close-by.

In the open ocean, the SWIFT drift velocity v_S is a combination of wind drift, wave-induced Stokes drift, and inertial currents. Typical drift speeds are $|v_S| \ll 1$m/s at angles relative to the dominant wave propagation $\theta_S < 30^o$. For a better comparison with the observations at fixed location, we correct the dominant wave frequency observed by SWIFTs $\tilde{\omega}_p$ for the effect of the drift

$$\omega_p = \tilde{\omega}_p + k_p\,|v_S|\,\cos(\theta_S) \tag{7}$$

prior to calculating the dominant wave length via the dispersion relation (6).

In addition, a 0.9 m Datawell DWR MKIII directional waverider moored at Station P (CDIP166, and NDBC 46246) yields H_s as well as directional wave spectra based on 20-min acquisition records. The waverider collects buoy pitch, roll, and heave displacements at 1.28 Hz on a 30-min duty cycle, following the Datawell standards. Both types of buoys process data onboard at the end of each duty cycle

and transmit the spectral moments to servers on shore via Iridium satellites.

2.3 Wave model

The numerical wave model used here is WAVEWATCH III ® (TWDG2014), with the physics package of Ardhuin et al. (2010). The geographic grid is global, at 0.5 degree resolution, and the spectral grid includes 36 directional bins and 31 frequency bins (0.0418 to 0.72 Hz, logarithmically spaced). An obstruction grid is used to represent unresolved islands (TWDG2014). Winds and ice concentrations are taken from the Navy Global Environmental Model (NAVGEM) (Hogan and Coauthors 2014), with the former input at 3-h intervals and the latter at 12-h intervals. The simulation is initialized 0000 UTC 1 December 2014 and ends 0000 UTC 1 February 2015. With invalid spin-up time removed, the valid portion of the simulation is 0000 UTC 15 December 2014 to 0000 UTC 1 February 2015. The physics package of Ardhuin et al. (2010) requires specification of a parameter, β_{max} which is used to compensate for the mean bias of the input wind fields, or lack thereof; $\beta_{max} = 1.2$ is used for this hindcast. The model version number employed is development version 5.04. In context of the present application, this is not substantially different from public release version 4.18.

H_s is calculated as 4 times the square root of the total sea surface variance, which is the integral of the variance density spectrum, which is the prognostic variable of the model. The dominant wave length λ_p is calculated using the linear dispersion relation for deep water using peak frequency f_p, which is calculated within the model using a parabolic fit around the discrete peak of the one-dimensional frequency spectrum (for details, see TWDG2014). The peak direction' is the mean direction of the peak frequency. The mean direction is arctan(b_1/a_1), where a_1 and b_1 are $a_1(f_p)$ and $b_1(f_p)$, the Fourier coefficients of the directional spreading function at the peak frequency (see e.g., Longuet-Higgins et al. (1963)) . It is important to note that this 'peak direction' is calculated in the same way as for the waverider and the SWIFTs. However, 'peak directions' from the model and the buoys are therefore neither the peak of the 2-D directional spectrum nor the peak of the 1-D directional spectrum.

3 Results

The first TerraSAR-X overpass occurred on January 1, 2015 at 16:04 UTC, during the passing of a storm north of the site. Winds had shifted from southerly winds prior to 9:00 UTC to north-westerly direction starting around 12:00 UTC. The analysis of the SAR images shows a gradual increase of wave height from $H_s \approx 2.3$ m at the southern end of the swath to $H_s \approx 3.3$ m about 100 km further north (Fig. 2). The increase in wave height coincides with a similar gradual increase of wind speed from $u \approx 10.5$ m/s in the southern region to $u \approx 13$ m/s in the north, indicating that the wave field is predominantly a local wind-generated sea.

The SAR-retrieved wave heights are in good agreement with the in situ observations obtained from three SWIFT buoys and the waverider. However, the in situ observations were spaced too closely to make any inference about the spatial evolution of the wave field. Wind speeds retrieved from the SAR image and wind speeds utilized for the wave model are consistent and are about $20 - 25$ % higher than reported by the SWIFTs. The SWIFT anemometer is only 1 m above the surface, and wind speeds have not been adjusted to the standard 10 m reporting height. Wave heights obtained from the wave model capture the gradual south - to

Fig. 2 Fields of significant wave height H_s (*left*) and wind speed u (*right*) on 1 January 2015, retrieved from TerraSAR-X images. Individual symbols give location and values as obtained from SWIFT buoys (*red triangle*), waverider (*green x*), and results from the wave model (*black,o*)
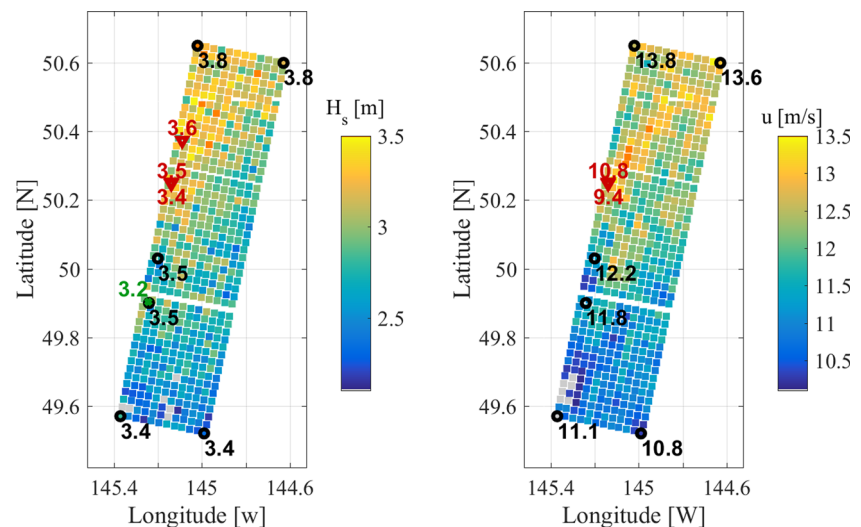
Fig. 3 Fields of dominant wave length λ_p (*left*) and dominant wave direction θ_p (*right*) on 1 January 2015, retrieved from TerraSAR-X images. Individual symbols give location and values as obtained from SWIFT buoys (*red tringle*), waverider (*green x*), and results from the wave model (*black,o*)
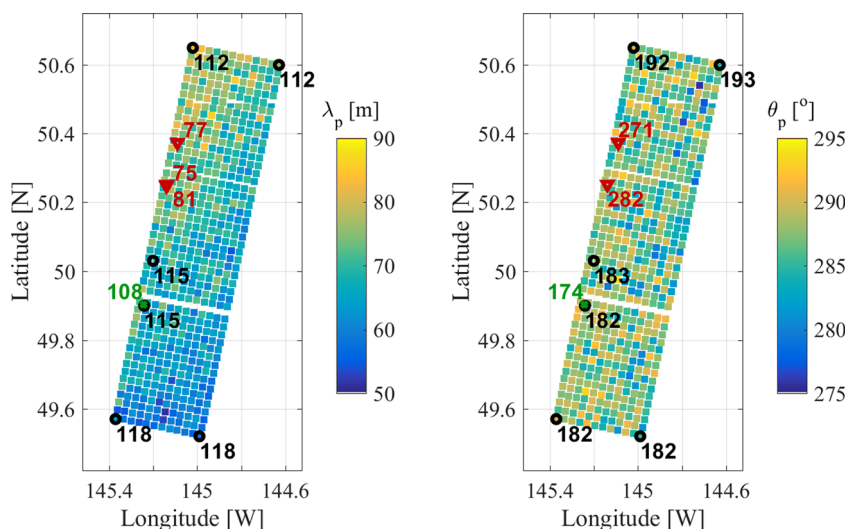
- north increase, but with a smaller gradient and generally higher values: $3.4\,\mathrm{m} \le H_s \le 3.8\,\mathrm{m}$.

The dominant wave length λ_p and dominant wave direction θ_p are indirect parameters related to a measure of the spectral maximum. Open ocean wave fields commonly consist of the superposition of several wave fields of different spectral strength, which can result in multi-peaked spectra. The SAR-retrieved dominant wave parameters as given by the maximum of the 2-D image spectrum shows rather short wave lengths increasing from $\lambda_p \approx 60\,\mathrm{m}$ in the south to $\lambda_p \approx 75\,\mathrm{m}$ in the north, at a direction of about 285° (Fig. 3). Contrary to the trend obtained from the SAR-image, the wave model predicts a much longer dominant wave length of $\lambda_p \approx 115\,\mathrm{m}$, slightly decreasing from south to north. The buoy observations yield intermediate wave lengths of $\lambda_p \approx 80\,\mathrm{m}$ from the SWIFT buoys and $\lambda_p = 108\,\mathrm{m}$ from the waverider buoy, with no clear spatial trend. Thus, depending on the data source, vastly different dominant wave lengths and reversed trends can be obtained. Furthermore, as will be discussed in more detail below, the definition of the dominant wave scale depends on the spectral analysis method,

and results will differ for different methods. The differences between the various observations are even more pronounced for the dominant wave direction. According to the SAR analysis and the SWIFT observations, the dominant wave direction is from WNW, $\theta_p \approx 290^o$, whereas the wave rider and the model show waves from S, $\theta_p \approx 170^o$ to 190° (Fig. 3).

The second TerraSAR-X overpass, 5 January 2015, 03:30 UTC, extents about 80 km along-track. Easterly winds at about $14\,m/s$ prevailed, with little variation over the imaged region (Fig. 4). The SAR image indicates H_s values of about $3.5\,\mathrm{m}$ south of 50^oN sharply increasing to $H_s \approx 4.4\,\mathrm{m}$ in the northern section of the image. This division of the wave field is also seen in the dominant wave length, jumping from $\lambda_p \approx 80\,\mathrm{m}$ in the south to $\lambda_p \approx 200\,\mathrm{m}$ in the north, and a shift in dominant wave direction from $\theta \approx 90^o$ to $\theta \approx 50^o$ (Fig. 5). There was one SWIFT within the southern section of the SAR image and another 3 SWIFTs about 25 km west of the central image section. Reported H_s values vary from 3.8 m in the south to 4.1 m outside the central section, roughly consistent with the values and

Fig. 4 Fields of significant wave height H_s (*left*) and wind speed u (*right*) on 5 January 2015, retrieved from TerraSAR-X images. Individual symbols give location and values as obtained from SWIFT buoys (*red triangle*), waverider (*green x*), and results from the wave model (*black,o*)
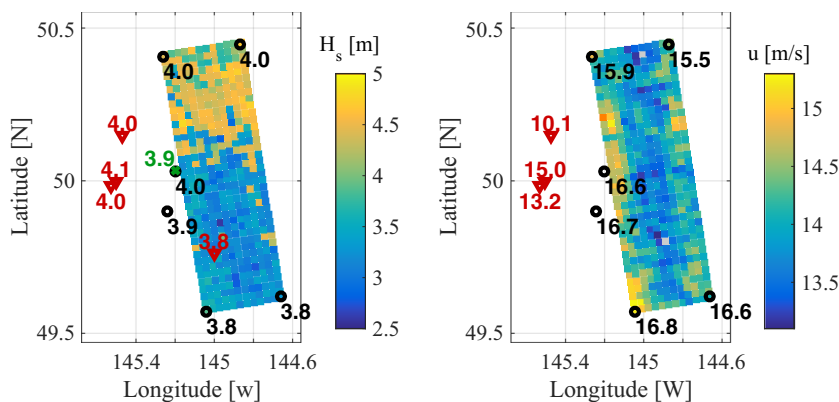
Fig. 5 Fields of dominant wave length λ_p (*left*) and dominant wave direction θ_p (*right*) on 5 January 2015, retrieved from TerraSAR-X images. Individual symbols give location and values as obtained from SWIFT buoys (*red triangle*), waverider (*green x*), and results from the wave model (*black,o*)
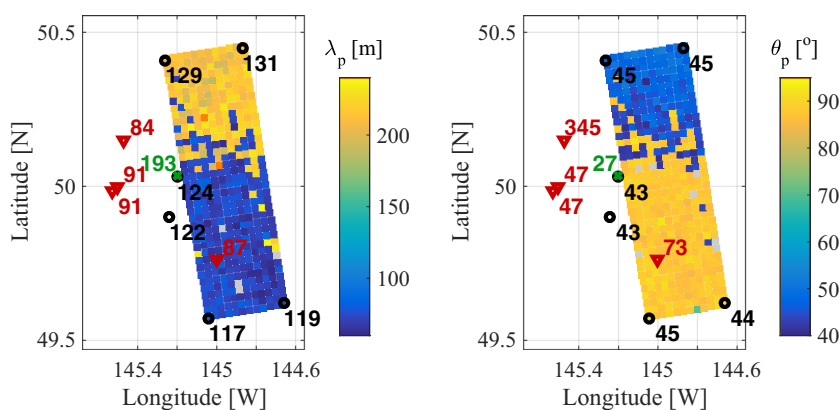
spatial pattern obtained from the SAR images. Results from different SWIFTs less than 1 km apart vary by 0.1 m, indicating $\Delta H_s \leq 0.1$ m is the uncertainty inherent in these 30-min wave observations. Modeled wave heights increase from $H_s = 3.8$ m in the south to $H_s = 4.0$ m in the north, supporting the increase, but not the relatively sharp jump, in wave height retrieved from the SAR image. In general, wave models do have an inherent tendency of smoothing sharp gradients. The modeled wave spectra and, thus, wave heights, are a result of spatial and temporal integration of the effect of the wind field on the waves, together with advection. The integration naturally produces smoothing, and the winds themselves are already smooth, as they do not have the resolution to predict sub-mesoscale features in the atmosphere.

Only the SAR-retrieved wave field suggests the division of easterly, wind-sea dominated waves in the south, and north-easterly swell in the north, due to a relative shift of spectral energy (Fig. 6). All SWIFTs report wind seas with $\lambda_p \approx 90$ m, but a change in dominant wave direction from $\theta_p = 73^o$ in the southern section to $\theta_p = 47^o$ and 345° west and northwest of the SAR image. The wave model predicts a complex sea state consistent of multiple systems. Reducing this multi-modal system to single dominant parameters can give misleading values. Here, the resulting dominant wave lengths fall between the wind sea and swell with $\lambda_p \approx 120$ m in the south, increasing to $\lambda_p \approx 130$ m at the northern edge of the SAR image, and $\theta_p \approx 45^o$ (Fig. 5). Overall, in both examples, the significant wave heights obtained from the four data sources agree relatively well. Reducing multi-peaked directional spectra to "dominant parameters" leads to noticeable differences in dominant wave direction and in peak wave length. As discussed below, this also leads to significant differences in wave steepness.

4 Discussion

The comparison of the SAR-retrieved wave parameters to the in situ and the modeled wave parameters revealed some

significant differences, in particular when dealing with dominant scales. Historically, most wave measurements are obtained as time series at a fixed location. Therefore, best practices are defined in the time domain, and wave scales are based on frequency, rather than wave number space. For spatial wave observations at a fixed time, H_s estimates might be expected to depend on the survey area, as well as the directional spreading and crest length of the wave field.

Based on the dispersion relation, wave parameters of individual waves may readily be expressed in temporal or
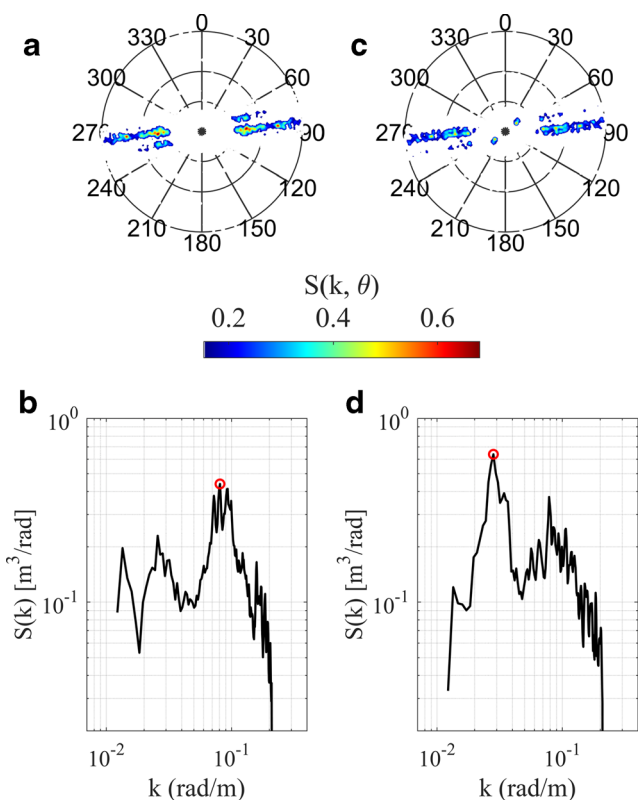
Fig. 6 Image spectra on 5 January 2015; **a** and **b** for southern section at 49.64°N, 144.88°W, and **c, d** for northern section 50.39°N, 145.07°W

spatial description. However, for a spectrum of wave scales, the dominant parameters do not readily convert (Gebhardt et al. 2015). Thus, the question arises what are best practices for obtaining wave field parameters from spatial observations, and what are the limitations of assessing spatial algorithms with the help of temporal observations, or vice versa.

4.1 Observational record size

Significant wave height is defined as the average of the highest one third waves within a record. For a random sea with a Gaussian distribution of surface elevations, this is within 1 % error the same as $H_s = 4\sigma_\eta$, where σ_η is the standard deviation of the surface elevation time series. However, even for stationary wave records, the result will fluctuate depending on the the record length. We simulate a 10-h-long stationary surface elevation record for a fully developed sea (Gemmrich and Garrett 2011), and calculate H_s values at the beginning of each hour, but with varying acquisition lengths from 10 min to 1 h, each yielding 10 estimates for H_s (Fig. 7). The average value of H_s is in all cases within 1 % of the correct value specified in the simulation. However, for the shortest acquisition (10 minutes), the estimates span a range of > 20 %, more than twice the uncertainty
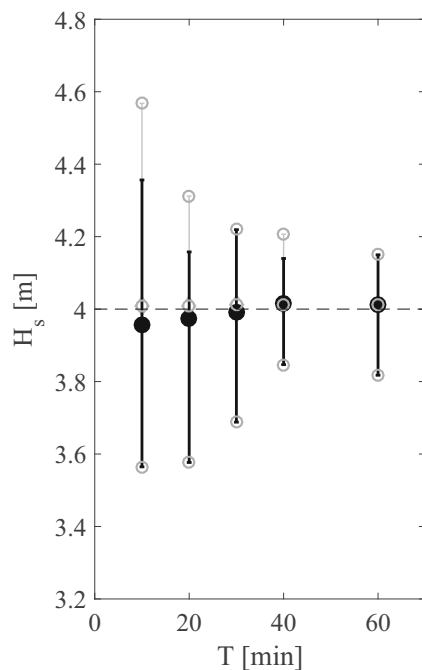
obtained for acquisition lengths $T \geq 40$ min. Conversely, one could consider calculating H_s from all consecutive data sections for the entire data record, thus increasing the number of independent estimates for acquisition times $T <$ 1 hour. For all acquisition lengths, the average H_s value is 4 m. However, for the shortest acquisition, the estimates span a range of 3.56 m $\leq H_s \leq$ 4.57 m. Uncertainties seem to stabilize at $\approx$ 10 % for acquisition length $T > 30$ min.

A recent study examined the statistical uncertainty of wave height and wave period estimated from waverider observations in the North Sea (Bitner-Gregersen and Magnusson 2014). They found the variability of wave height estimates to be greater than the uncertainty in wave periods. They also point out that "sampling variability of H_s may have a significant impact on (...) validation of different data sources and wave models".

Taking $T_p = 10$ s as a typical dominant wave period, the standard operational acquisition length of 38 min (Environment Canada) yields about $N_t = 225$ dominant waves as the basis for estimating wave field parameters. Therefore, it would be desirable to base the analysis of spatial records on a similar number of waves $N_s \approx N_t$. For unidirectional, long-crested waves, an equivalent spatial acquisition size of length $L_a = N_s\lambda_p$ and arbitrary width could be defined. However, for directional, short-crested wave fields commonly observed at mid-latitude open ocean locations, it is generally not known how many independent dominant wave crests are contained within an acquisition area $L_a \times L_a$. Here, we compare H_s, and λ_p estimates obtained from our standard acquisition area with $L_a = 2560$ m to to estimates based on acquisition areas with $L_a = 5120$ m. For convenience, we assume $N_s = (L_a/\lambda_p)^2$ as an upper bound for the number of independent dominant waves within the acquisition area.

On 1 January 2015, the dominant wave length was about 70 m, yielding $N_s \gg N_t$ for both sizes of the acquisition area. Thus, there is no systematic difference of the H_s estimates between the two acquisition sizes (Fig. 8a), and for the majority of the estimates the difference is $|\Delta H_s| \leq$ 0.2 m (Fig. 8c). On 5 January 2015, the influence of longer swell prevailed in the northern section of the observational area, with $\lambda_p \approx 220$ m, yielding $N_s \gg N_t$ only for the larger acquisition area, but $N_s \ll N_t$ for $L_a = 2560$ m. For the northern section, where $H_s > 4$ m, estimates obtained from the smaller (*i.e.* standard) acquisition are clearly biased toward lower wave heights (Fig. 8b). Individual differences reach $|\Delta H_s| > 1$ m, but again the majority of the estimates are in the range $|\Delta H_s| \leq 0.2$ m (Fig. 8d).

For both datasets, dominant wave length and dominant direction do not show a systematic dependence on record size (not shown). However, in the 5 January 2015 data, the peak jumps occasionally from the dominant wind sea to the dominant swell.

Fig. 7 Variability of significant wave height H_s as function of acquisition period T. *Black errorbars* give range of H_s calculated from 10 sections with same starting time but different length. *Gray circles* show the range for all consecutive records. All H_s estimates are based on the same simulated, stationary surface elevation time series
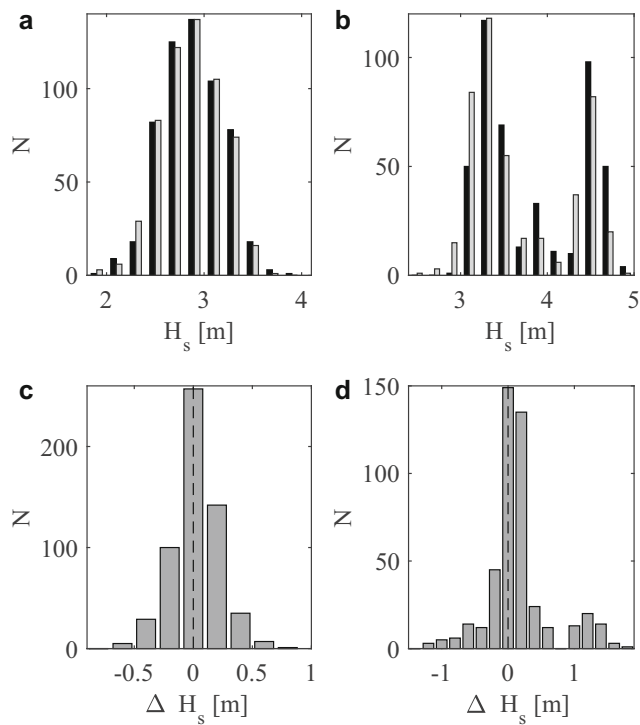
Fig. 8 *Top* Variability of significant wave height H_s over entire image area, for acquisition areas of 2560 m × 2560 m (*gray*) and 5120 m × 5120 m (*black*). *Bottom*: Difference of H_s estimates between 5120 m × 5120 m and 2560 m × 2560 m acquisitions. For 1 January 2015 (**a**), (**c**) and 5 January 2015 (**b**), (**d**)

4.2 Dominant wave scale

Viewing TerraSAR-X imagery of the open ocean scenes one can often readily determine by eye a dominant wave length and a dominant wave direction. The equivalent data analysis

method is to determine the location k_p, θ_p of the peak of the two-dimensional wave number spectrum $S(k, \theta)$ (Fig. 1a). Integrating the 2-D spectrum over all directions gives the 1-D wave number spectrum (Fig. 1b). For most wave fields, the dominant wave length $\lambda_p = 2\pi/k_p$ from the 2-D and 1-D wavenumber spectra match. However, there are situations where the integration can lead to a different dominant scale. For example, assume two moderate swell systems with similar wave lengths but different directions and a wind sea that is stronger than either of the swell systems; the sum of the swell systems can have a higher 1-D peak than the wind sea and the dominant wave scale would jump from the wind sea as obtained from the 2-D spectrum to the dominant scale of the swell. The opposite case, where the peak of the longer waves dominates the 2-D spectra, but shorter waves are the most energetic directionally-integrated scales occurred on 5 January 2015 (Fig. 9a,b). In the southern part of the observations, both methods are in good agreement, whereas in the northern section, there is a clear division of scales.

For temporal wave observations, the dominant scale is defined as the peak of the frequency spectrum (Fig. 1c). This situation can be emulated from a 2-D wavenumber spectrum via the dispersion relation and the Jacobian ($k \, \partial k/\partial \omega$). Due to this conversion, the peak in frequency space corresponds to slightly reduced peak wave lengths (Gebhardt et al. 2015). This effect can clearly be seen in the dataset of 5 January 2015, where frequency-based wave lengths are systematically shorter than the dominant wave scale obtained in 1-D and 2-D wave number space (Fig. 9c).

Dominant wave parameters in the wave model are calculated from various moments and weights of spectral energy (e.g., TWDG2014), ensuring a smooth evolution of wave parameters in time and space. For comparison with the

Fig. 9 Comparison of dominant wave length λ_p on 5 January 2015, derived from TerraSAR-X images based on 2-D wave number spectra (**a**), 1-D wave number spectra (**b**), and 1-D frequency spectra (**c**). *Gray colour scale* depicts swell, ranging from 190 to 240m (dark to light)
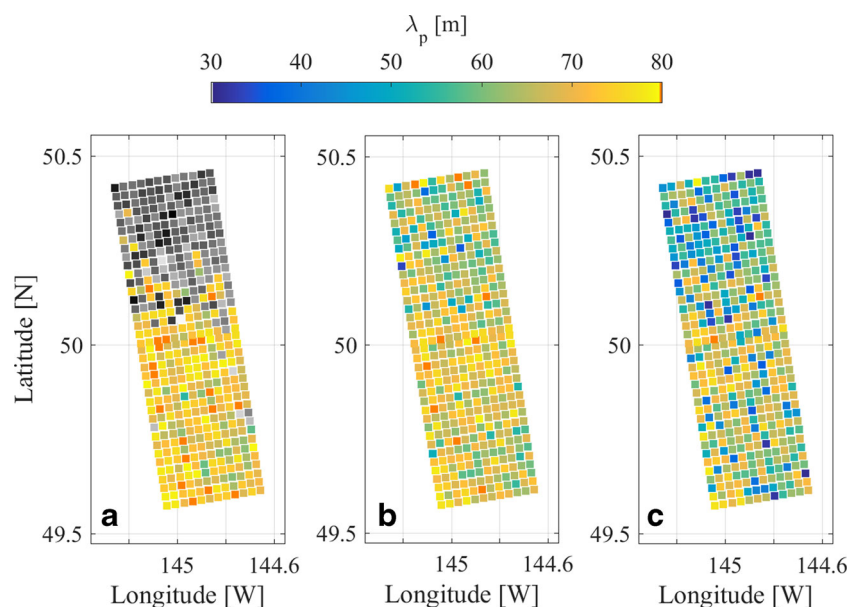
SAR-retrieved parameters, more direct estimates might be desirable. Therefore, we calculate different estimates of dominant wave parameters directly from the model output spectra, along a transect through the SAR images at 145W (Fig. 10). The dominant wave length is obtained via the dispersion relation from estimates of the peak wave period T_p. Here, we include the standard wave model output T_{mm10}, as well as the peak of the 1-d frequency and the 2-D frequency-direction spectra. In terms of wave length, the results can vary by up to $\Delta\lambda_p = 80$ m, but all estimates are larger than the SAR analysis, and the SWIFT buoys, suggest. The dominant wave direction in the model is commonly calculated as the mean direction of the wave components of the dominant frequency. In addition, we extract the direction from the peak of the modeled 2-D wave spectra. Both methods agree within 30° with each other, but can be vastly different

from the SAR and SWIFT results. This is likely due to the smoothing and relative coarse directional resolution inherent in the model result. The significant wave height has contributions from all spectral components, rather than only a small subsection like dominant period or direction. Differences in H_s between the model and the observations are therefore mainly due to the coarse spatial resolution of the model.

Depending on the data source and the processing method the results for the dominant wave lengths can vary by almost a factor of 2. In addition, for multi-peaked wave systems, the dominant scale can jump between peaks of similar strength. This has huge implications on the dominant steepness H_s/λ_p. For moderate sea states, it is often the steepness of a wave field rather than the absolute wave height that determines marine risks. Furthermore, dominant steepness is used as first-order predictor of breaking rates of dominant waves (Banner et al. 2000) and, thus, air-sea exchange processes. However, the overall wave breaking rate and the associated turbulence levels also depend on the steepness in the saturation range of the spectrum, and mean-square slope or the related wave saturation, are better indicators of breaking than dominant steepness (Banner et al. 2002; Schwendeman et al. 2014; Schwendeman and Thomson 2015).

For pure wind seas, the "3/2 power law" predicts $H_s \propto T_p^{3/2}$ (Toba 1972), where T_p is the peak wave period. Utilizing the deep water dispersion relation (6) this is equivalent to

$$H_s \propto \lambda_p^{3/4}. \tag{8}$$

Although our two datasets include swell components, they are mainly dominated by developing wind sea, and Eq. 8 can provide a consistency check. For 1 January 2015 waves in the northern section, where $H_s \geq 3.0$ m, agree well with the "3/2 power law", and SAR-retrieved wave parameters and SWIFT results are consistent. Model-based wave steepness are significantly less, and do not indicate a coherent spatial wave evolution (Fig. 11a). Surprisingly, the waverider gives an intermediate wave steepness, lower than the estimates from SWIFT and SAR. The waverider internal processing includes a coarse low-pass filter of the 1-d frequency spectrum. It is likely that the peak at an intermediate frequency is the result of the smoothing and coarse resolution of the spectrum, rather than being caused by difference in the observational technique.

The second dataset, 5 January 2015, is characterized by wind sea in the southern section and swell-dominated seas in the northern part. Wave lengths retrieved in the 2-D wave number space in the wind sea section closely follow the evolution curve. Wave parameters from SWIFT are on the same steepness curve but at greater wave development (Fig. 11b). The waverider is located in the transition between wind sea and swell-dominated region and the energy at the lower
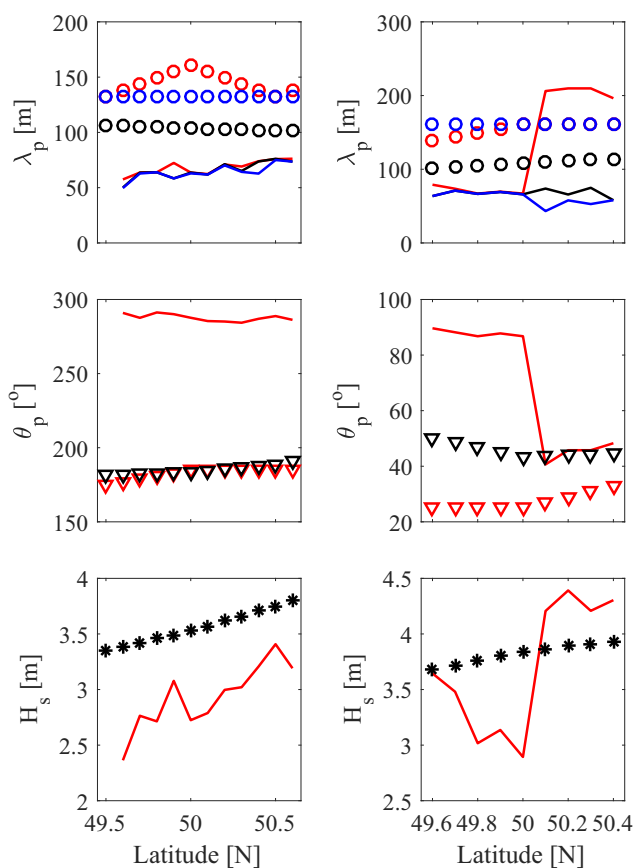
Fig. 10 Comparison of dominant wave parameters based on different definitions, from model results (*symbols*) and from SAR image analysis (*line*), along a cross section at 145W. *Left column* 1 January 2015, *right column:*5 January 2015. *Top row* Dominant wave length λ_p from standard model output (*black circles*), from 2-D spectra (*red circles*), from 1-D spectra (*blue circles*), from 1-D k-spectra (*black line*), from 2-D k-spectra (*red line*), and from 1-D ω-spectra (*blue line*). *Middle row* Dominant wave direction θ_p from 2-D frequency spectra (*red triangles*), from 1-D spectra (*black triangles*), and from 2-D k-spectra (*red line*). *Bottom row* Significant wave height H_s

Fig. 11 Comparison of significant wave height H_s as function of dominant wave length λ_p for different data sources and methods: SWIFT buoys (*red* $\triangledown$), waverider (*green* $\times$), wave model (*black,$\circ$*), TerraSAR-X images based on 2-D wave number spectra (*blue*), 1-D wave number spectra (*gray* $\times$), and 1-D frequency spectra (*orange $\diamond$*). *Dashed lines* give wave height evolution $H_s \propto \lambda_p^{3/4}$ for normalized initial steepness 1, 0.5 and 0.33 (*left to right*) (Toba 1972). **a** 1 January 2015, **b** 5 January 2015
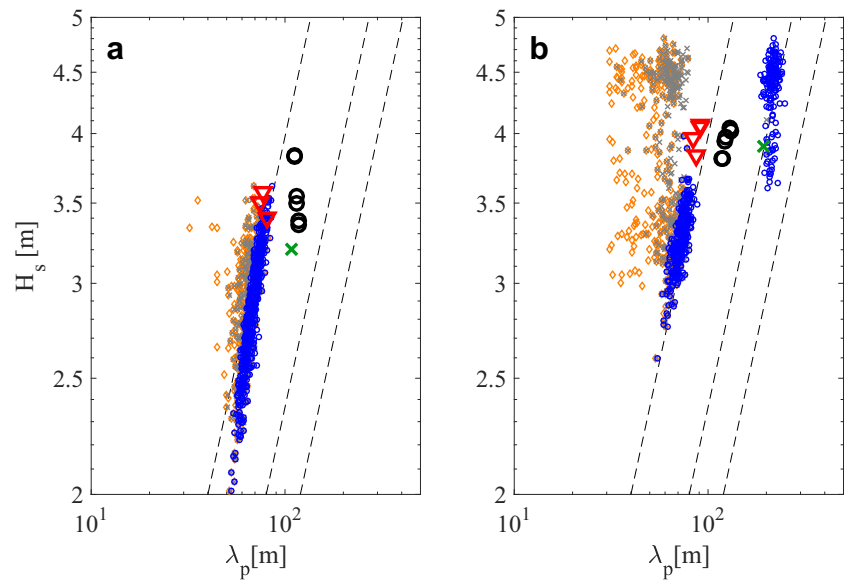
frequency is slightly higher than the energy in the frequency range corresponding to the wind sea (not shown). Thus, the waverider, and the SAR results from the northern section with $H_s > 3.5$ m, have the lowest steepness of all data sources. These data are swell dominated and do not show a spatial wave evolution. Peak wave lengths from the SAR 1-D spectra are in the wind sea range over the entire image. However, they are roughly constant, and do not indicate wave evolution, even for the southern section. The wave model predicts an evolving wave field, but at about 60 % of the steepness measured by SWIFTs or TerraSAR-X. Based on these results, the retrieval of dominant wave scales from the 2-D wave number space is recommended.

5 Conclusions

Dominant wave field parameters are estimated based on a certain observations record size. Due to the random nature of oceanic wave fields, these parameters possess an inherent uncertainty which decreases with increasing record length. For spatial observations and pure wind seas, a standard acquisition area of $2.5\,km \times 2.5\,km$ seems to be appropriate. However, for mixed wind seas and swell, a larger area is recommended. For point observations of a stationary wave field, estimates of significant wave heights based on 30-min time series have about half the uncertainty compared to estimates from a 10-min record length. Spectral differences in wave number and frequency space lead to slightly different dominant wave scales from time series or spatial wave observations. The reduction of complex multi-system sea states to single dominant parameters can yield huge uncertainties in dominant wave length and direction. These natural and introduced fluctuations should be kept in

mind in comparison of different observational methods or in model validation studies.

Nevertheless, wave fields in the open ocean can include true wave height variations that exceed the measurement uncertainty at spatial scales of O (10 km), stressing the need for co-located observations for the assessment of model results or empirical wave retrieval algorithm. Satellite-borne SAR imagery is an ideal tool to retrieve such meso-scale wave field changes, which tend to be smeared out in operational wave predictions.

The next step will be to explain the physics of these relatively abrupt wave field fluctuations. They seem not associated with spatial pattern in wind speed. We speculate, wave modulations by inertial currents might be a contributing factor (Gemmrich and Garrett 2012).

References

Ardhuin F et al. (2010) Semi-empirical dissipation source functions for ocean waves: Part I, definitions, calibration and validations. J Phys Oceanogr 40:1917–194

Banner ML, Babanin AV, Young IR (2000) Breaking probability for dominant waves on the sea surface. J Phys Oceanogr 30(12):3145–3160

Banner ML, Gemmrich JR, Farmer DM (2002) Multiscale measurements of ocean wave breaking probability. J Phys Oceanogr 32(12):3364–3375

Bitner-Gregersen EM, Magnusson AK (2014) Effect of intrinsic and sampling variability on wave parameters and wave statistics. Ocean Dyn 64:1643–1655

Bruck M (2015) Sea state measurements using TerraSAR-X / Tandem-X. Ph.D. thesis, University Kiel

Bruck M, Lehner S (2013) Coastal wave field extraction using TerraSAR-X data. J Appl Remote Sens 7. doi:10.1117/1.JRS.7.073,694

Gebhardt C, Pleskachevsky A, Rosenthal W, Lehner S, Hoffmann P, Kieser J, Bruins T (2015) Comparing wavelength simulated by coastal wave model CWAM and TerraSAR-X satellite data. Ocean Model

Gemmrich J, Garrett C (2011) Dynamical and statistical explanations of observed occurrence rates of rogue waves. Nat Hazards Earth Syst Sci 11:1437–1446

Gemmrich J, Garrett C (2012) The signature of inertial and tidal currents in offshore wave records. J Phys Oceanogr 42. doi:10.1175/JPO–D–12–043.1

Heller EJ (2006) Freak ocean waves and refraction of Gaussian seas, pp. 189–210. Springer

Herbers THC, Jessen P, Janssen T, Colbert D, MacMahan JH (2012) Observing ocean surface waves with gps tracked buoys. J Atmos Ocean Tech 29. doi:10.1175/JTECH–D–11–00,128.1

Hogan T, Coauthors (2014) The navy global environmental model. Oceanograph 27:116–125

Koch W (2004) Directional analysis of SAR images aiming at wind direction. IEEE Trans Geosci Remote Sens

Lehner S, Pleskachevsky A, Velotto D, Jacobsen S (2014) Meteo-marine parameters and their variability observed by high-resolution satellite radar images. Oceanography 26:81–91

Longuet-Higgins MS, Cartwright DE, Smith ND (1963) Observations of the directional spectrum of sea waves using the motions of a floating buoy., Conference on Ocean Wave Spectra, Ed., Prentice Hall

Pleskachevsky A, Rosenthal W, Lehner S (2016) Meteo-marine parameters for highly variable environment in coastal regions from satellite radar images. ISPRS Journal of Photogrammetry and Remote Sensing, doi:10.1016/j.isprsjprs.2016.02.001

Ren ASL, Brusch YS, Li X, He M (2012) An algorithm for the retrieval of sea surface wind fields using X-band TerraSAR-X data. Int J Remote Sens 33:7310–7336

Schwendeman M, Thomson J (2015) Observations of whitecap coverage and the relation to wind stress, wave slope, and turbulent dissipation. doi:10.1002/2015JC011196

Schwendeman M, Thomson J, Gemmrich J (2014) Wave breaking dissipation in a fetch limited seas. J Phys Oceanogr 44:104–127

Thomson J (2012) Wave breaking dissipation observed with swift drifters. J Atmos Ocean Tech 29:1866–1882

Thomson J, Schwendeman MS, Zippel SF, Moghimi S, Gemmrich J, Rogers E (2016) Wave breaking turbulence in the ocean surface layer

Toba Y (1972) Local balance in the air-sea boundary processes: I. on the growth process of wind waves. J Oceanogr Soc Jpn 28:15–26

Tolman H, the WAVEWATCH III Development Group (2014) User manual and system documentation of WAVEWATCH III, version 4.18, National Oceanic and Atmospheric Administration National Weather Service National Centers for Environmental Prediction, 5830 University Research Court College Park, MD, 20740